Seasonal dependence of geomagnetic active-time northern high-latitude upper thermospheric winds

Manbharat S. Dhadly[1], John T. Emmert[2], Douglas P. Drob[2], Mark G. Conde[3], Eelco Doornbos[4], Gordon G. Shepherd[5], Jonathan J. Makela[6], Qian Wu[7], Rick J. Niciejewski[8], and Aaron J. Ridley[8]

[1]National Research Council Postdoctoral Research Associate, Space Science Division, Naval Research Laboratory, Washington DC, USA
[2]Space Science Division, Naval Research Laboratory, Washington DC, USA
[3]Geophysical Institute, University of Alaska Fairbanks, Alaska, USA
[4]Aerospace Engineering, Delft University of Technology, The Netherlands
[5]Centre for Research in Earth and Space Science, York University, Canada
[6]Department of Electrical and Computer Engineering, University of Illinois at Urbana-Champaign, Illinois, USA
[7]High Altitude Observatory, UCAR, Colorado, USA
[8]Climate and Space Sciences and Engineering, University of Michigan, Ann Arbor, Michigan, USA

Key Points:

- Investigating the large-scale seasonal dependence of geomagnetic active-time northern high-latitude upper thermospheric winds.
- The latitudinal extent of duskside circulation expands almost ten degrees from winter to summer.
- Comparisons with Disturbance Wind Model (DWM07) suggest that DWM07 winds are skewed toward summertime conditions.

This is the author manuscript accepted for publication and has undergone full peer review but has not been through the copyediting, typesetting, pagination and proofreading process, which may lead to differences between this version and the Version of Record. Please cite this article as doi: 10.1002/2017JA024715

Corresponding author: Manbharat Dhadly, manbharat.dhadly.ctr@nrl.navy.mil

Abstract
This study is focused on improving the poorly understood seasonal dependence of northern high-latitude *F* region thermospheric winds under active geomagnetic conditions. The gaps in our understanding of the dynamic high-latitude thermosphere are largely due to the sparseness of thermospheric wind measurements. With current observational facilities, it is infeasible to construct a synoptic picture of thermospheric winds, but enough data with wide spatial and temporal coverage have accumulated to construct a meaningful statistical analysis. We use long-term data from eight ground-based and two space-based instruments to derive climatological wind patterns as a function of magnetic local time, magnetic latitude, and season. These diverse data sets possess different geometries and different spatial and solar activity coverage. The major challenge is to combine these disparate data sets into a coherent picture while overcoming the sampling limitations and biases among them. In our previous study (focused on quiet-time winds), we found bias in the GOCE cross-track winds. Here, we empirically quantify the GOCE bias and use it as a correction profile for removing apparent bias before empirical wind formulation. The assimilated wind patterns exhibit all major characteristics of high-latitude neutral circulation. The latitudinal extent of duskside circulation expands almost ten degrees from winter to summer. The dawnside circulation subsides from winter to summer. Disturbance winds derived from geomagnetic active and quiet winds show strong seasonal and latitudinal variability. Comparisons between wind patterns derived here and Disturbance Wind Model (DWM07) (which have no seasonal dependence) suggest that DWM07 is skewed toward summertime conditions.

1 Introduction

The high-latitude thermospheric wind is a key regulator of the coupled magnetosphere-ionosphere-thermosphere system. It is the primary redistributor of the energy deposited from the magnetosphere [e.g., *Mayr and Harris*, 1978; *Killeen et al.*, 1986; *Burns et al.*, 1991, 1995; *Sutton*, 2016; *Dhadly and Conde*, 2017]. The large-scale high-latitude thermospheric wind circulation is predominantly driven by dayside solar heating, ion-drag, inertial forces (Coriolis and centrifugal), and other heating sources such as Joule heating and particle precipitation [e.g., *Meriwether et al.*, 1973; *Thayer and Killeen*, 1993; *Richmond et al.*, 2003; *Kwak and Richmond*, 2007]. These energy and momentum sources show strong variations with geomagnetic activity, interplanetary magnetic field (IMF) strength and orientation, solar activity, and season [e.g., *Hernandez and Roble*, 1976; *Babcock and Evans*, 1979; *McCormac and Smith*, 1984; *McCormac et al.*, 1987; *Rees and Fuller-Rowell*, 1989; *Sica et al.*, 1989; *Aruliah et al.*, 1991, 1996; *Niciejewski et al.*, 1992; *Killeen et al.*, 1995; *Emmert et al.*, 2006a,b; *Wu et al.*, 2008; *Förster et al.*, 2008; *Dhadly and Conde*, 2016]. Therefore, thermospheric wind also changes with changes in these drivers.

Although high-latitude geospace wind has been studied for decades, its large-scale response to space weather drivers is observationally still poorly characterized. Recently, *Dhadly et al.* [2017] studied the large-scale seasonal response of geomagnetically quiet-time (here referred to as "quiet-time study") polar cap, auroral, and mid latitude upper thermospheric winds in the Northern Hemisphere. In this paper, we statistically characterize the large-scale seasonal response when geomagnetic conditions are active (herein called "active-time", defined by $K_p \geq 3$). We also examine the seasonal dependence of the difference between active-time and quiet-time wind ("disturbance wind"). The basic underlying structure and technical implementation of this study is similar to the quiet-time study with some important additions and improvements.

During active geomagnetic conditions, the magnetosphere dumps a large amount of energy in the high-latitude upper atmosphere and disturbs the ionosphere-thermosphere system. At these times, using current global observational facilities, accurate specifications (let alone predictions) of the global thermospheric wind field are difficult to obtain.

This is primarily because wind measurements are obtained either from sparsely located ground-based Fabry-Perot spectrometers (FPS) or space-based instruments. The ground-based data sets provide limited spatial coverage but extended nighttime temporal coverage. On the other hand, space-based techniques provide wide global coverage with limited daytime as well as nighttime temporal coverage. Due to the lack of comprehensive space-time coverage of thermospheric wind observations, our current understanding of the seasonal dependence is based on several regional statistical studies and on simulations by first-principles models [e.g., *Hernandez and Roble*, 1976; *Babcock and Evans*, 1979; *Aruliah et al.*, 1991, 1996; *Fuller-Rowell et al.*, 1996; *Emmert et al.*, 2006a; *Deng et al.*, 2014; *Cnossen and Förster*, 2016]. The sparseness of data has hampered scientific progress in understanding global circulation. The problem is much more acute at high latitudes due to the complexity of the dynamics there.

Thermospheric wind data sets are still sparse, but enough data have accumulated to permit meaningful statistical analysis of northern high-latitude horizontal winds as a function of season, magnetic latitude (MLAT), and magnetic local time (MLT) for geomagnetically quiet and active conditions. To obtain a systematic seasonal characterization of the large-scale upper thermospheric neutral wind circulation from middle to polar latitudes in the Northern Hemisphere, this study uses a diversity of long-term historical observations from eight ground-based (optical remote sensing) and two space-based (optical remote sensing and in situ) instruments, and combines their daytime and nighttime measurements into a coherent empirical representation of vector winds as a function of season, magnetic latitude, and magnetic local time. These diverse data sets possess different geometries and different spatial and solar coverage. The major challenge of the effort is to combine these disparate sources of data into a coherent picture while overcoming the sampling limitations and biases among the data sets. The problem is dimensionally complex: The average winds may depend on latitude and local time, universal time (or, equivalently, longitude), day of year, solar activity, geomagnetic activity, and IMF configuration. Instrumental bias adds an additional dimension.

Emmert et al. [2008] studied the behavior of storm-induced disturbance winds as a function of geomagnetic activity and codified the Disturbance Wind Model (DWM07), which is the storm-time component of the Horizontal Wind Model (HWM14) [*Drob et al.*, 2015]. DWM07 does not account for any seasonal dependence of high-latitude geospace winds. Utilizing the results of the present active-time study and our previous quiet-time study, we calculate the disturbance winds, examine their seasonal dependence, and compare with DWM07.

In this paper, we describe the data used in this study (section 2), analysis and fitting procedures (section 3), validation of resulting empirical models (section 4), model results (section 5), and conclusions (section 6). At F region altitudes, the quantities of vorticity and divergence provide important insight into the primary drivers of neutral circulation and the coupling between the ionosphere and thermosphere. Thus, in addition to the seasonal dependence of active-time winds and disturbance winds, this study also characterizes the seasonal behavior of the active-time large-scale vorticity and divergence patterns. Many aspects of this study are similar to our quiet-time study (*Dhadly et al.* [2017]). Therefore, only key figures are included in the main body of this paper. Additional figures and discussion are included in the supporting information.

2 Observational Data

Table 1 summarizes the instruments, their locations, temporal and spatial data coverage, contributing data points, and references used. This study includes long-term (spanning 1983 to 2015) historic active-time upper thermospheric wind data recorded by a space-based optical remote sensing instrument (WIND Imaging Interferometer (WINDII) on the Upper Atmosphere Research Satellite (UARS)), one in-situ space-based accelerom-

eteră(Gravity Field and Steady-State Ocean Circulation Explorer (GOCE) accelerometer), and eight ground-based optical remote sensing Fabry-Perot spectrometers (FPS) located at various latitudes above 45N MLAT. Out of these eight ground-based FPSs, two are wide field Scanning Doppler imaging Fabry-Perot interferometers (SDIs) located inside the auroral zone and six are narrow field Fabry-Perot interferometers (FPIs) located at various latitudes from the polar cap to middle latitudes. Space-based data from all latitudes are included in our assimilations in order to stabilize our spherical harmonic fits; however, we only examine results above 45N MLAT.

The data recorded by these instruments come from a broad range of thermospheric *F* region altitudes. Both the FPI and SDI techniques, which measure the Doppler shift in 630 nm airglow emissions, assume that the peak emission altitude is centered around 240-250 km and that vertical wind gradients are insignificant. However, at high latitudes, the peak altitude of 630 nm airglow emission can vary many tens of kilometers about the centroid. The altitude of the in situ GOCE measurements varied between 253 km and 295 km. UARS WINDII recorded data (daytime winds at 557.7 nm and nighttime at 630.0 nm) from a wide range of altitudes from the upper to lower thermosphere. WINDII filter selections were determined more on a short term campaign basis than a single long-term synoptic day/night side setup. Based on the various altitudes measured by the different techniques, we selected data in the altitude range of 210-320 km. our results represent the height-averaged seasonal dependence of *F* region thermospheric winds. *Killeen et al.* [1982], *Wharton et al.* [1984], and *Emmert et al.* [2002] have demonstrated that there is no statistically significant altitude variation in measured climatological wind speed at *F* region altitudes.

The available data span 1983 to 2015 with daily 10.7 cm solar radio flux ($F_{10.7}$) varying between 60 sfu and 400 sfu (1 sfu = 10^{-22} $Wm^{-2}Hz^{-1}$). The dependence of high-latitude thermospheric winds on solar flux is poorly understood; as a precaution to minimize such effects on our seasonal analysis, we used wind measurements from each instrument when solar flux conditions were quiet to moderate (defined by $F_{10.7} \leq 150$). Table 1 summarizes the average $F_{10.7}$ of the selected data points for each instrument. The average $F_{10.7}$ for the selected data in December solstice, equinox, and June solstice bins are 110 sfu, 106 sfu, and 106 sfu, respectively. The small difference among these average $F_{10.7}$ values suggests that any dependence of the winds on solar flux should not alias into the estimated seasonal dependence.

The data used here are obtained from multiple instruments operated independently; they have different technical implementations, modes of operations, data processing algorithms, and spatial and temporal sampling. For example, the SDI instruments located at Poker Flat and Toolik Lake in Alaska measure upper thermospheric winds at high temporal and spatial cadence, resulting in a dense swath of wind measurements at latitudes covering 60–74N MLAT [e.g., *Dhadly et al.*, 2015]. To prevent those data sets from dominating our statistical wind model, we de-weighted these data sets by randomly selecting only 5%ă of their data for December solstice and equinox conditions. Similarly, GOCE produced a very dense swath of measurements around the dawn and dusk periods; its data set was de-weighted by taking a random 10% ăsubset in the December solstice, 3.3% during equinox, and 6.6% ăin June solstice. These sample population sizes were chosen to produce robust wind fits, as verified in section 4.

Additional details about the instruments and data sets are provided in *Dhadly et al.* [2017]. The distribution of the selected active-time wind data for this study as a function of magnetic latitude and magnetic local time, and for each of the three seasonal bins, is shown in Figure 1. All magnetic local times and magnetic latitudes are sufficiently covered during December solstice and equinox conditions, but in June solstice, only the dayside sector has full coverage. Dayside measurements are from space-based instruments and nighttime measurements are from both the space-based and ground-based instruments.

3 Methodology for Model Development

Because of the diversity of data sets included here, they possibly have mutual biases. *Dhadly et al.* [2017] compared various quiet-time data sets from the instruments included here and found no major biases among them except for GOCE. On the duskside, GOCE quiet-time cross-track winds are typically ~85 m/s larger (more eastward) on average than the corresponding component of quiet-time WINDII green line winds. Potential instrumental and data processing biases were ignored in *Dhadly et al.* [2017]. It is important to note that the GOCE wind measurements are not direct observations, but are derived from acceleration measurements, by making use of a model of the satellite aerodynamics *Doornbos et al.* [2010]. Systematic wind errors could therefore result from uncertainties in the aerodynamic model, specifically in the gas-surface interaction and satellite geometry parts of this model. Improvements to the GOCE aerodynamic model might therefore reduce such errors in the future, and such improvements are currently under investigation.

Because the MLAT dependence of the GOCE offsets with respect to the other data sets is consistent among different MLT and seasonal bins (refer to Figure 7 and 8 of *Dhadly et al.* [2017]), we estimate the bias in the GOCE cross-track wind measurements as a function of MLAT, as follows:

1. Produce a low resolution (order 10 and degree 3) quiet-time empirical wind climatology (following the procedure discussed in *Dhadly et al.* [2017]) as a function of MLAT and MLT by combining December solstice and equinox data, excluding GOCE data.
2. Bin and average quiet-time GOCE cross-track winds as a function of magnetic latitude for various magnetic local times by combining December solstice and equinox data.
3. Evaluate the the reference climatology at the GOCE measurement locations, and bin and average the resulting vector winds in the same way as the previous step.
4. Project binned and averaged quiet-time reference winds along the GOCE cross-track wind direction and subtract from the binned and averaged quiet-time GOCE cross-track winds to compute the average difference as a function of MLAT for several MLT bins, as shown in Figure S1.
5. Average these MLAT difference profiles shown in Figure S1 over all the MLT bins to obtain a single bias profile as a function of MLAT, as shown in Figure 2.
6. Evaluate the bias profile at each GOCE measurement location (via linear interpolation of the values shown in Figure 2), and subtract the bias from all the GOCE cross-track measurements (quiet and active, and including June solstice data) to obtain a corrected GOCE data set.

The estimated GOCE bias correction profile is very general and does not eradicate all the discrepancies between GOCE and the other data sets (discussed in section 4). However, it contains the most discernible trend present in the GOCE bias. The aerodynamic model parameters and the magnetic latitude dependent pointing of the satellite with respect to the wind flow, determine the amount of aerodynamic lift that is generated in the aerodynamic model of the satellite. A small change in the aerodynamic model parameters and the way the satellite is pointing with respect to the wind flow as a function of magnetic latitude can introduce such errors in the cross-track wind derivation from GOCE accelerations. If a future improvement to the GOCE aerodynamic model used in the GOCE wind data processing reduces the offset, this would become the preferred solution. .

The uncorrected GOCE winds as a function of magnetic latitude show very similar wind characteristics as observed by the other high-latitude wind measuring instruments (illustrated in *Dhadly et al.* [2017] model validation section); however, the magnitudes of winds are different. Thus, the GOCE correction does not simply amplify any trends in the other high-latitude wind data. The motivation behind GOCE bias correction is to make

best possible use of the GOCE data when data availability from the other instruments is very limited, such as in the summer season.

For the purpose of this study, we selected active-time observational data defined by 3-hour planetary $K_p \geq 3$ and then divided into three broad seasonal bins: December solstice (Nov, Dec, Jan, Feb), equinox (Mar, Apr, Sep, Oct), and June solstice (May, Jun, Jul, Aug). For discussion purposes, the latitudes considered in this study are divided into three categories: 80–90N MLAT as polar cap latitudes, 60–80N MLAT as auroral latitudes, and 45–60N MLAT as middle latitudes.

The details of methodology and wind assimilation technique used here are discussed in *Dhadly et al.* [2017] and *Emmert et al.* [2008]. Briefly, we used vector spherical harmonic (VSH) functions as the basis of empirical representation of the observed active-time thermospheric winds as a function of season, MLAT, and MLT. In the high-latitude geospace environment, neutral motions are better organized in magnetic coordinates [*Hays et al.*, 1984; *Richmond*, 1995; *Emmert et al.*, 2008, 2010]; thus, for an efficient characterization of the high-latitude geospace wind system, we assimilated thermospheric winds in quasi-dipole magnetic coordinates [*Richmond et al.*, 2003; *Emmert et al.*, 2008, 2010]. The available active-time wind data as function of season, MLAT, and MLT supports VSH expansion at degree 10 in magnetic latitude and order 3 in magnetic local time. VSH coefficients based on ordinary least square fits were calculated using data from each seasonal bin. The spatial resolution is lower than the quiet-time fits in *Dhadly et al.* [2017] (degree 17, order 5) because in the present study the data coverage is sparser especially in summer. Calculating thermospheric statistical wind fits at the lower resolution prevents spurious oscillations in wind fits in the regions where data are limited. Although this lower model resolution likely smoothes out the sharp gradients that exist at the equatorward boundary of the auroral zone, it produces a more robust seasonal analysis. We applied the same quality control procedures described in *Dhadly et al.* [2017].

Given that *Dhadly et al.* [2017] has developed the quiet-time seasonal climatology of northern high-latitude neutral winds and the present study examines their active-time seasonal behavior, storm-time induced perturbations (disturbance winds) can be estimated as a function of season, MLAT, and MLT from the results of these two studies. The underlying procedure for calculating disturbance winds is similar to that of *Emmert et al.* [2008], except that *Emmert et al.* [2008] calculated separate quiet-time baselines for each data set. We computed a quiet-time (K_p <3) seasonal climatology at the same resolution (degree 10, order 3) as the active time climatology (and also using the corrected GOCE data) and subtracted it from the active-time modeled winds for each season to obtain disturbance winds, which we then compared with the DWM07 of *Emmert et al.* [2008].

4 Model Validation

In this section, we evaluate the modeled active-time seasonal winds by comparing modeled climatology with the observational data used in its formulation. The primarily focus of this section is to 1) check if the model can adequately reproduce salient features of the high-latitude neutral winds evident in the data, 2) investigate the model robustness in the space-time regions of limited data availability, and 3) identify any biases among the diverse active-time wind data sets. Only the highlights of the model validation results are presented in the main text; additional details are provided in the supporting information, including Figures S2-S9, which we will refer to in this section.

As illustrated in Figures S2-S6, the active-time empirical wind morphology closely matches the observations and reproduces salient features of high-latitude neutral wind circulation, with a few minor discrepancies (discussed in the following paragraphs). These comparisons suggest no major biases among various data sets. The daytime wind climatology is primarily driven by space-based data, while nighttime is by ground-based data.

The combined daytime (space-based) and nighttime observational data (space-based and ground-based) matches closely without any obvious discontinuity in the dawnside winds and duskside winds as a function of magnetic local time.

In the equinox 16–20 MLT sector, zonal winds measured by WINDII (green line) are more westward than winds from the ground-based stations PF SDI and TL SDI (Figure S5). This MLT bin compares the daytime WINDII green line winds and nighttime SDI winds. The WINDII data are mostly from days closer to the summer season, while the SDI data are from days closer to the winter solstice (refer to Figure S9). Thus, the difference in WINDII and SDI zonal winds in this MLT bin probably arises from a seasonal dependence, rather than a mutual bias. Ionospheric conductance associated with photoionization (solar driven conductance) is usually higher under sunlit condition than non-sunlit conditions [*Moen and Brekke*, 1993; *Ridley*, 2007]. The stronger neutral winds under sunlit conditions may be associated with the enhanced ionization, which increases the ion drag force on the neutrals. It suggests that at the same location in MLT–MLAT space in the auroral zone, active-time wind dynamics can be significantly different in sunlit conditions than in non-sunlit conditions.

Model average and WINDII climatology are in good agreement at mid latitudes, but discrepancies arise at and above auroral latitudes (Figure S5 and S6). Some differences exist between the model climatology and WINDII daytime data in 08–16 MLT bins notably in the winter and equinox. In this time range, binned average model climatology appears to be underestimating the latitudinal gradients that exist in the zonal winds at auroral latitudes. Strong latitudinal gradients in the zonal winds are a characteristic feature of high-latitude neutral wind circulation. High spectral resolution is required to fit these gradients to a high degree of accuracy. Furthermore, sufficient data coverage is required at all locations, otherwise the model can introduce spurious oscillations in the regions with limited data availability.

WINDII red line measurements show strong variability in zonal and meridional winds. The cause of this variability in WINDII nighttime winds is currently unknown. Overall, the WINDII nighttime winds present similar winds morphology within the limits of uncertainty as observed by ground-based stations.

The larger differences between the modeled zonal wind climatology in summer and other two seasons between 60–80 MLAT around magnetic midnight (between 20–24 MLT and 00–02 MLT) could be attributed to a lack of data in this region.

The corrected GOCE cross-track winds are generally in good agreement with the cross-track winds derived from WINDII, SDIs, FPIs, and model climatology (refer to Figures S7 and S8). On the average, GOCE cross-track winds on the duskside are ~21 m/s, 10 m/s, and 41 m/s more positive (more eastward) than WINDII green line cross-track winds in winter, equinox, and summer, respectively. In the quiet-time study, these differences were ~89 m/s, 73 m/s, and 87 m/s in winter, equinox, and summer, respectively. Although, there are still discrepancies between GOCE and other data sets, the above calculated differences and Figure S7 and S8 suggest compelling overall improvements in the GOCE cross-track winds and model results, after application of the GOCE corrections.

To quantify how the distribution of data (especially the large summer gaps) affects the uncertainty of the modeled average winds (at the model resolution), we estimated 1σ uncertainty in the modeled zonal and meridional winds as a function of magnetic local time and magnetic latitude for each season (shown in Figure S10). The estimated 1σ uncertainty in the modeled zonal winds averaged over the entire MLT-MLAT space for December solstice, equinox, and June solstice are 1.7 m/s, 1.9 m/s, and 4.3 m/s, respectively. For meridional winds, the average estimated uncertainties for December solstice, equinox, and June solstice are 1.8 m/s, 2.0 m/s, and 4.5 m/s, respectively.

5 Results and Discussion

The behavior of the modeled wind climatology is satisfactory (as discussed in section 4) within the limits of its resolution and hence can be used to investigate the large-scale seasonal behavior of thermospheric wind circulation as a function of magnetic latitude and magnetic local time. This section discusses the response of active-time high-latitude *F* region thermospheric winds to the change in seasons utilizing the observational data and calculated empirical wind fits. In addition, the seasonal dependence of disturbance winds derived from quiet-time and active-time winds are discussed.

5.1 Seasonal Dependence of Active-time Winds

At high latitudes, solar illumination varies strongly with the change in seasons; these latitudes stay mostly sunlit in summer and dark in winter. Consequently, the solar driven processes in the upper thermosphere and ionosphere contribute directly and indirectly to the seasonal variability of mean thermospheric wind circulation. Also, any seasonal dependence of high-latitude particle precipitation can alter the coupling between the ionosphere and thermosphere via ion drag, and hence the behavior of neutral winds.

Figure 3 shows the polar plots of assimilated vector winds for each season (winter, equinox, and summer) as a function of magnetic latitude and magnetic local time. It illustrates the dominance of rotational flow in the mean neutral wind circulation. The results show all the major characteristic features of convection-dominated high-latitude neutral wind circulation such as a strong duskside circulation cell, strong antisunward winds in the polar cap, sharp latitudinal gradients in the duskside auroral zone associated with zonal wind reversal at convection boundaries, and a weaker dawnside circulation cell. Active-time winds are stronger than winds from the quiet-time study, as expected. There are marked seasonal differences in the mean neutral wind circulation: The overall intensity of mean wind circulation increases from winter to summer.

Another difference between quiet-time and active-time circulation is the equatorward expansion of active-time duskside circulation from winter to summer. The wind reversal region at the equatorward edge of the auroral zone (due to the transition from magnetic westward ion drag to eastward (antisunward) solar pressure gradient dominated wind flows) marks the boundary of the duskside circulation cell. This sharp wind reversal makes it one of the most dynamic regions of the thermosphere. Figure 4 shows the location of the zonal wind reversal and reveals that the duskside circulation expands approximately ten degrees equatorward from winter to summer. Reversal boundaries were also calculated for dawnside circulation; their movement indicate a poleward retreat of dawnside circulation from summer to winter.

To study the details of seasonal dependence, Figure 5 shows two-dimensional wind maps of each wind component (zonal and meridional) as a function of magnetic latitude and magnetic local time for each season. A direct comparison between fitted winds from the three seasons is shown in Figure 6. Together, Figures 3-6 summarize the major results of this study. Overall, the winds are stronger in summer than in winter, and the seasonal dependence tends to increase with increasing latitude.

In addition to the shift of the zonal wind reversal boundary, the equatorward expansion of the dusk cell from winter to summer also manifests at middle latitudes as a shift toward more westward winds. This can be seen in Figure 6 as well as in the average winds from the PM, MH, and UR FPIs shown in Figure S4. The average zonal winds in the duskside (14–22 MLT) middle latitudes shift from 27 m/s (positive eastward) in winter to -73 m/s (negative westward) in summer.

The intensification of the duskside circulation from winter to summer can be clearly interpreted from the fully developed duskside circulation cell. The dawnside circulation is

always much weaker than the duskside circulation and its complete cycle is rarely, if ever, observed. Thus, its existence is smeared in the mean neutral circulation. Nevertheless, the tendency of antisunward winds to turn dawnward in the post-magnetic midnight sector 0000-0600 MLT suggests the consistent effect of dawnside convection on neutrals. Here we have interpreted the strength of neutral dawnside circulation from the eastward component of zonal winds. Overall, this eastward tendency in the zonal winds subsides from winter to summer and zonal winds completely turn westward in summer. Any signature of the dawnside circulation is completely wiped out by the strong antisunward polar jets. This gradual turning of zonal winds in this MLAT-MLT sector suggests the subsidence of dawnside circulation from winter to summer. This behavior is similar to the quiet-time seasonal dependence and suggests that in the summer time, neutrals passing through the throat region (where solar pressure gradient and ion-drag forces are in same direction) gain enough momentum to thwart the effect of ion-drag (with the help of Coriolis force, which increases with speed) to draw them into the dawnside circulation cell.

Zonal winds primarily show a diurnal character (two extrema in the MLT variation) at polar and middle latitudes (~45–50 MLAT), and a semidiurnal character (four extrema) at auroral latitudes (refer to Figure 6). The average seasonal trend in zonal winds is similar on the dawnside at all latitudes. The enhancement in westward zonal wind on the duskside (~18–22 MLT) at auroral latitude is predominantly the signature of ion-neutral coupling (via ion drag) that usually exists at auroral latitudes. The zonal wind channeling through the auroral zone on the duskside shows a strong dependence on season (Figure 5), with the depth of trough deepening from winter to summer. This is consistent with the WINDII green line observations shown in Figure S5. The average speed of magnetic westward zonal winds in the duskside (14–22 MLT) auroral zone increases from 54 m/s in winter to 187 m/s in summer. In the post-magnetic midnight (00–06 MLT) winter and equinox seasons, zonal winds are eastward between 55–75 MLAT. The eastward component in this MLAT–MLT region is most likely associated with the dawnside ionospheric plasma convection. Overall, this eastward tendency of zonal winds subsides from winter to summer and zonal winds completely turn westward in summer (Figure 6). Similar behavior on the dawnside was observed in quiet-time winds by *Dhadly et al.* [2017]. The average eastward zonal winds in the dawnside (00-06 MLT) auroral zone changes from 27 m/s in winter to -106 m/s in summer. Similar behavior was observed at middle latitudes, where zonal winds on the dawnside (00–06 MLT) change from 23 m/s in winter to -73 m/s in summer.

Meridional winds show a diurnal character at all the latitudes considered in this study (Figure 6). In the polar cap, strong meridional winds around magnetic noon and midnight are associated with antisunward polar jets; the strength of meridional winds decreases with decreasing latitude. The strength of latitudinal gradients in meridional winds also decreases with decreasing latitudes, but it increases from winter to summer. The average antisunward meridional winds in the polar cap increase from ~129 m/s in winter to 197 m/s in summer. Overall, the seasonal difference in meridional winds diminishes with decreasing latitude.

At *F* region altitudes, ion drag is one of the primary drivers of vorticity, which makes vorticity a good dynamical measure of the coupling between the ionosphere and thermosphere. Divergence in neutral wind fields is primarily driven by heating induced pressure gradients, Coriolis force, and non-convective forces. Thus, vorticity and divergence are two important parameters of high-latitude neutral wind circulation and can provide some critical insights into the drivers of high-latitude neutral circulation [e.g., *Mayr and Harris*, 1978; *Volland*, 1979; *Hays et al.*, 1984; *Thayer and Killeen*, 1991, 1993; *Förster et al.*, 2011; *Kwak and Richmond*, 2014]. The seasonal dependence of the active-time vorticity and divergence is very similar to that of the quiet-time results presented by *Dhadly et al.* [2017]. *Dhadly et al.* [2017] also discuss the basic science and general behaviors in vorticity and divergence of horizontal wind fields. We use the coefficients of VSH wind

fits to calculate the vorticity (vertical component) and divergence of average F region horizontal wind fields for each season. In the northern hemisphere, negative vorticity corresponds to anticyclonic rotation (clockwise circulation) and positive vorticity corresponds to cyclonic rotation (anticlockwise circulation). The calculated vorticity maps as a function of magnetic latitude and magnetic local time for northern high-latitude wind circulation under active geomagnetic conditions depicted in Figure 7, clearly illustrate the formation of the well-known anticyclonic vortex on the duskside and cyclonic vortex on the dawnside. Vorticity in the dusk sector is mostly related to shear and curvature in wind field, while vorticity in the dawn sector is mostly due to the latitudinal gradients in the zonal winds. The general pattern of the vorticity derived here matches with the pattern presented by *Thayer and Killeen* [1991]. The science of the formation of typical vorticity cells (duskside and dawnside votices) and diveregence in horizontal wind fields is described by *Thayer and Killeen* [1991], *Thayer and Killeen* [1993], *Förster et al.* [2011], *Kwak and Richmond* [2014], and *Dhadly et al.* [2017]. As a better metric for examining the seasonal dependence of high-latitude vorticity, we focus only on the duskside and dawnside circulation vortices bounded by the black curves (as shown in Figure 7, top row) and calculated the average vorticity (weighted by cosine latitude) within each bounded cell. The average anticyclonic vorticity of the duskside cell increases from -103×10^{-6} s^{-1} in winter to -124×10^{-6} s^{-1} in equinox to -187×10^{-6} s^{-1} in summer. In contrast, the cyclonic vorticity of the dawnside cell shows a small decrease from winter to summer: 75×10^{-6} s^{-1} in winter, 68×10^{-6} s^{-1} in equinox, and 64×10^{-6} s^{-1} in summer. Because ion drag is the primary driver of high-latitude vorticity, this suggests that ion-neutral coupling increases on the duskside from winter to summer, whereas it slightly decreases on the dawnside from winter to summer. The average absolute vorticity over the entire region in winter, equinox, and summer is 68×10^{-6} s^{-1}, 87×10^{-6} s^{-1}, and 127×10^{-6} s^{-1} respectively. It indicates overall increase in vorticity from winter to summer. This suggests that overall dynamic coupling between the ionosphere and thermosphere maximizes in summer. Vorticity patterns show slight clockwise tilt from the noon-midnight meridian; this tilt is strongest in equinox. Figure 7 (bottom row) shows the large-scale divergence maps as a magnetic latitude, and magnetic local time. Similar to vorticity, overall divergence shows a progressive increase from winter to summer, although the seasonal dependence of divergence is weaker than that of vorticity. In all the seasons, the strongest divergences occur around and above auroral latitudes. The average absolute divergence over the entire region considered in this study in winter, equinox, and summer is 22×10^{-6} s^{-1}, 32×10^{-6} s^{-1}, and 35×10^{-6} s^{-1}, respectively.

5.2 Seasonal Dependence of Disturbance Winds

Storm induced wind disturbances for each season at high latitudes are calculated by subtracting quiet-time winds from active-time winds. The resulting high-latitude disturbance vector winds are presented in Figure 8. Overall, the wind patterns are dominated by anticyclonic rotation, with progressive intensification from winter to summer, especially on the duskside. In all the seasons, disturbance winds are stronger on the duskside than on the dawnside. Also, shown in Figure 8 (last panel) are corresponding results from DWM07, which we ran for K_p=3.9, which is the average value for the data used in this study. The mean neutral circulation in the summertime disturbance winds closely resembles the DWM07 patterns, which suggests a significant contribution of strong active summertime winds to the DWM07 derived disturbance winds. To further explore this possibility, a direct comparison of the zonal and meridional disturbance wind components derived here and from DWM07 is presented in Figure 9. The average winds calculated by combining disturbance winds from all the three seasons are also shown. Overall, although disturbance winds and DWM07 winds present similar behaviors, DWM07 is often closer to the summer disturbance wind curves than to the seasonally averaged curves. In particular, DWM07 meridional winds closely follow the meridional June disturbance winds. On the duskside, zonal disturbance winds follow closely DWM07 zonal winds, while on the

dawnside, the DWM07 zonal winds are more similar to the seasonally averaged results. This comparison indicates that DWM07 winds tend to behave more like summertime disturbance winds than any of the other seasons.

6 Conclusions

We examined the large-scale seasonal dependence of the northern high-latitude *F* region thermospheric wind circulation under active geomagnetic conditions. The ground-based and space-based neutral wind observations as a function of season, magnetic latitude, and magnetic local time were combined to assimilate a comprehensive seasonal picture of the high-latitude geospace wind system. The ground-based data sets provided extensive nighttime coverage, whereas space-based instruments were the primary daytime data sets. We found no major biases among various data sets used here except for GOCE. Because of the similar nature of the bias present in the GOCE cross-track winds as a function of MLAT for various MLT bins, we statistically quantified the apparent GOCE bias as a function of MLAT and applied it as a correction profile to the GOCE measurements. Observed differences of up to 100 m/s between WINDII daytime and SDI nighttime winds during equinox at the same location in MLT–MLAT space in the auroral zone strongly suggest that active-time wind dynamics can be significantly different in sunlit conditions than in non-sunlit conditions.

Overall, the active-time assimilated wind morphology is in good agreement with the observational data and captures most of the climatological variations evident in the data used in its formulation. The results show that significant changes occur in the active-time high-latitude wind behavior with the change in seasons. The most significant changes occur at auroral and polar latitudes. Overall, the mean high-latitude neutral wind circulation is strongest in the summer season and weakest in the winter season. The duskside anticyclonic circulation shows strong intensification from winter to summer, whereas the dawnside anticyclonic circulation subsides from winter to summer. In terms of individual wind components, zonal winds at auroral latitudes and meridional winds in the polar cap exhibit strong seasonal dependence. The strength of westward zonal winds channeling through the auroral zone is much stronger in summer (~187 m/s) compared to winter (~54 m/s). Westward flow intensifies and expands to lower latitudes from winter to summer. On the dawnside, average zonal wind speed (auroral and middle latitudes) changes from 25 m/s eastward in winter to 90 m/s westward in summer. Similarly, antisunward winds in the polar cap are much stronger in summer (~197 m/s) than in winter (~129 m/s). The location of wind reversal boundary on the duskside under active geomagnetic conditions moves almost ten degree equatorward from winter to summer with the expansion of duskside circulation cell. Such expansion was not observed in the quiet-time circulation.

The winds from three middle latitude stations show a progressive shift in zonal wind from eastward to westward from winter to summer. The average active-time zonal wind in the duskside middle latitudes changes from 27 m/s eastward in winter to 73 m/s westward in summer. The strength of latitudinal gradients in meridional winds decreases with decreasing latitudes but increases from winter to summer. Comparison with quiet-time wind climatology shows that during active-time conditions the middle latitude meridional winds are similar to the quiet-time winds, but the active-time zonal winds are much more westward than quiet-time winds.

We also studied the seasonal dependence of disturbance winds derived in a similar fashion as in DWM07 of *Emmert et al.* [2008]. In DWM07, no seasonal dependence of thermospheric winds was taken into consideration and data from all seasons were combined. The similarities between the summertime disturbance winds derived here and the DWM07 patters suggests that DWM07 is skewed towards summer conditions.

This study combined with *Dhadly et al.* [2017] presents a complete systematic study of the seasonal dependence of northern high-latitude neutral wind circulation. This multi-instrument study sets a necessary benchmark for validating new observations and tuning first-principles models. Previous studies of high latitudes thermospheric winds from individual stations [e.g., *Wu et al.*, 2008] have shown significant solar ($F_{10.7}$) dependence, but the response of high latitude neutral wind circulation to solar flux changes is still largely unknown. In a future study, we will utilize this seasonal climatology of winds to remove seasonal effects from the input data and examine their solar flux dependence. This is a part of an ongoing effort to improve the high-latitude performance of the Horizontal Wind Model (HWM14).

Acknowledgments

This study was supported by NASA's Heliophysics Supporting Research Program (grant NNH16AC381). This work was conducted while Manbharat Singh Dhadly held a National Research Council's Research Associateship at Naval Research Laboratory, Washington, DC. K_p and $F_{10.7}$ indexes are available at NASA OMNIWeb data explorer (https://omniweb.gsfc.nasa.gov/). Poker Flat and Toolik Lake SDI data are available at http://sdi server.gi.alaska.edu/sdiweb/index.asp. WINDII Level 2 data are available from Gordon Shepherd (gordon@yorku.ca). GOCE data can be obtained from https://earth.esa.int/web/guest/missions/esa-operational-missions/goce /goce-%20thermospheric-data. All other data sets can be obtained from the Madrigal database at http://cedar.openmadrigal.org/cgi-bin/accessData.cgi. Poker Flat and Toolik Lake SDI operations (during the observing periods included in this manuscript) were supported by the National Science Foundation through grant numbers AGS1243476, AGS1140075, and AGS0821431. Resolute Bay data was supported by the National Science Foundation through grant AGS1339918. Data collection for the Urbana and Peach Mountain FPIs was supported by the National Science Foundation through grants AGS 1452291 and ATM1452097.

References

Aruliah, A. L., D. Rees, and T. J. Fuller-Rowell (1991), The combined effect of solar and geomagnetic activity on high latitude thermospheric neutral winds. Part I. Observations, *J. Atmos. Terr. Phys.*, *53*(6–7), 467–483, doi:http://dx.doi.org/10.1016/0021-9169(91)90075-I.

Aruliah, A. L., A. D. Farmer, D. Rees, and U. Brändström (1996), The seasonal behavior of high-latitude thermospheric winds and ion velocities observed over one solar cycle, *J. Geophys. Res.*, *101*(A7), 15,701, doi:10.1029/96JA00360.

Babcock, R. R., and J. V. Evans (1979), Seasonal and solar cycle variations in the thermospheric circulation observed over Millstone Hill, *J. Geophys. Res.*, *84*(A12), 7348, doi:10.1029/JA084iA12p07348.

Burns, A. G., T. L. Killeen, and R. G. Roble (1991), A theoretical study of thermospheric composition perturbations during an impulsive geomagnetic storm, *J. Geophys. Res. Sp. Phys.*, *96*(A8), 14,153–14,167, doi:10.1029/91JA00678.

Burns, A. G., T. L. Killeen, G. R. Carignan, and R. G. Roble (1995), Large enhancements in the O/N 2 ratio in the evening sector of the winter hemisphere during geomagnetic storms, *J. Geophys. Res.*, *100*(A8), 14,661–14,671, doi:10.1029/94JA03235.

Cnossen, I., and M. Förster (2016), North-south asymmetries in the polar thermosphere-ionosphere system: Solar cycle and seasonal influences, *J. Geophys. Res. Sp. Phys.*, *121*(1), 612–627, doi:10.1002/2015JA021750.

Conde, M., and R. W. Smith (1995), Mapping thermospheric winds in the auroral zone, *Geophys. Res. Lett.*, *22*(22), 3019–3022, doi:10.1029/95GL02437.

Deng, Y., Y. Huang, Q. Wu, J. Noto, D. Drob, and R. B. Kerr (2014), Comparison of the neutral wind seasonal variation from midlatitude conjugate observations, *J. Geophys.*

Res. Sp. Phys., *119*(4), 3029–3035, doi:10.1002/2013JA019716.

Dhadly, M., and M. Conde (2017), Trajectories of thermospheric air parcels flowing over Alaska, reconstructed from ground-based wind measurements, *J. Geophys. Res. Sp. Phys.*, *122*(6), 6635–6651, doi:10.1002/2017JA024095.

Dhadly, M., J. Emmert, D. Drob, M. Conde, E. Doornbos, G. Shepherd, J. Makela, Q. Wu, R. Niciejewski, and A. Ridley (2017), Seasonal dependence of northern high-latitude upper thermospheric winds: A quiet time climatological study based on ground-based and space-based measurements, *J. Geophys. Res. Sp. Phys.*, *122*(2), 2619–2644, doi:10.1002/2016JA023688.

Dhadly, M. S., and M. Conde (2016), Distortion of thermospheric air masses by horizontal neutral winds over Poker Flat Alaska measured using an all-sky scanning Doppler imager, *J. Geophys. Res. Sp. Phys.*, *121*(1), 854–866, doi:10.1002/2015JA021800.

Dhadly, M. S., J. Meriwether, M. Conde, and D. Hampton (2015), First ever cross comparison of thermospheric wind measured by narrow- and wide-field optical Doppler spectroscopy, *J. Geophys. Res. Sp. Phys.*, *120*(11), 9683–9705, doi:10.1002/2015JA021316.

Doornbos, E., J. V. Den IJssel, H. Lühr, M. Förster, G. Koppenwallner, S. Bruinsma, E. Sutton, J. M. Forbes, F. Marcos, and F. Perosanz (2010), Neutral Density and Crosswind Determination from Arbitrarily Oriented Multiaxis Accelerometers on Satellites, *J. Spacecr. Rockets*, *47*(4), 580–589, doi:10.2514/1.48114.

Doornbos, E. N., S. L. Bruinsma, B. Fritsche, G. Koppenwallner, P. Visser, J. Van Den IJssel, and J. Teixeira da Encarnação (2014), GOCE+ Theme 3: Air density and wind retrieval using GOCE data final report, *Tech. Rep.*(4000102847/NL/EL, TU Delft, Netherlands).

Drob, D. P., J. T. Emmert, J. W. Meriwether, J. J. Makela, E. Doornbos, M. Conde, G. Hernandez, J. Noto, K. A. Zawdie, S. E. McDonald, J. D. Huba, and J. H. Klenzing (2015), An update to the Horizontal Wind Model (HWM): The quiet time thermosphere, *Earth Sp. Sci.*, *2*, doi:10.1002/2014EA000089.

Emmert, J. T., B. G. Fejer, G. G. Shepherd, and B. H. Solheim (2002), Altitude dependence of middle and low-latitude daytime thermospheric disturbance winds measured by WINDII, *J. Geophys. Res. Sp. Phys.*, *107*(A12), SIA 19–1–SIA 19–15, doi:10.1029/2002JA009646.

Emmert, J. T., M. L. Faivre, G. Hernandez, M. J. Jarvis, J. W. Meriwether, R. J. Niciejewski, D. P. Sipler, and C. A. Tepley (2006a), Climatologies of nighttime upper thermospheric winds measured by ground-based Fabry-Perot interferometers during geomagnetically quiet conditions: 1. Local time, latitudinal, seasonal, and solar cycle dependence, *J. Geophys. Res.*, *111*(A12), A12,302, doi:10.1029/2006JA011948.

Emmert, J. T., G. Hernandez, M. J. Jarvis, R. J. Niciejewski, D. P. Sipler, and S. Vennerstrom (2006b), Climatologies of nighttime upper thermospheric winds measured by ground-based Fabry-Perot interferometers during geomagnetically quiet conditions: 2. High-latitude circulation and interplanetary magnetic field dependence, *J. Geophys. Res.*, *111*(A12), A12,303, doi:10.1029/2006JA011949.

Emmert, J. T., D. P. Drob, G. G. Shepherd, G. Hernandez, M. J. Jarvis, J. W. Meriwether, R. J. Niciejewski, D. P. Sipler, and C. A. Tepley (2008), DWM07 global empirical model of upper thermospheric storm-induced disturbance winds, *J. Geophys. Res.*, *113*(A11), A11,319, doi:10.1029/2008JA013541.

Emmert, J. T., a. D. Richmond, and D. P. Drob (2010), A computationally compact representation of Magnetic-Apex and Quasi-Dipole coordinates with smooth base vectors, *J. Geophys. Res.*, *115*(A8), A08,322, doi:10.1029/2010JA015326.

Förster, M., S. Rentz, W. Köhler, H. Liu, and S. E. Haaland (2008), IMF dependence of high-latitude thermospheric wind pattern derived from CHAMP cross-track measurements, *Ann. Geophys.*, *26*(6), 1581–1595, doi:10.5194/angeo-26-1581-2008.

Förster, M., S. E. Haaland, and E. Doornbos (2011), Thermospheric vorticity at high geomagnetic latitudes from CHAMP data and its IMF dependence, *Ann. Geophys.*, *29*(1), 181–186, doi:10.5194/angeo-29-181-2011.

Fuller-Rowell, T. J., M. V. Codrescu, H. Rishbeth, R. J. Moffett, and S. Quegan (1996), On the seasonal response of the thermosphere and ionosphere to geomagnetic storms, *J. Geophys. Res.*, *101*(A2), 2343, doi:10.1029/95JA01614.

Hays, P. B., T. L. Killeen, N. W. Spencer, L. E. Wharton, R. G. Roble, B. A. Emery, T. J. Fuller-Rowell, D. Rees, L. A. Frank, and J. D. Craven (1984), Observations of the dynamics of the polar thermosphere, *J. Geophys. Res. Sp. Phys.*, *89*(A7), 5597–5612, doi: 10.1029/JA089iA07p05597.

Hernandez, G., and R. G. Roble (1976), Direct measurements of nighttime thermospheric winds and temperatures, 1. Seasonal variations during geomagnetic quiet periods, *J. Geophys. Res.*, *81*(13), 2065–2074, doi:10.1029/JA081i013p02065.

Killeen, T. L., P. B. Hays, N. W. Spencer, and L. E. Wharton (1982), Neutral winds in the polar thermosphere as measured from Dynamics Explorer, *Geophys. Res. Lett.*, *9*(9), 957–960, doi:10.1029/GL009i009p00957.

Killeen, T. L., R. G. Roble, R. W. Smith, N. W. Spencer, J. W. Meriwether, D. Rees, G. Hernandez, P. B. Hays, L. L. Cogger, D. P. Sipler, M. A. Biondi, and C. A. Tepley (1986), Mean neutral circulation in the winter polar F region, *J. Geophys. Res. Sp. Phys.*, *91*(A2), 1633–1649, doi:10.1029/JA091iA02p01633.

Killeen, T. L., Y.-I. Won, R. J. Niciejewski, and A. G. Burns (1995), Upper thermosphere winds and temperatures in the geomagnetic polar cap: Solar cycle, geomagnetic activity, and interplanetary magnetic field dependencies, *J. Geophys. Res.*, *100*(A11), 21,327, doi: 10.1029/95JA01208.

Kwak, Y. S., and A. D. Richmond (2007), An analysis of the momentum forcing in the high-latitude lower thermosphere, *J. Geophys. Res.*, *112*(A1), A01,306, doi: 10.1029/2006JA011910.

Kwak, Y. S., and A. D. Richmond (2014), Dependence of the high-latitude lower thermospheric wind vertical vorticity and horizontal divergence on the interplanetary magnetic field, *J. Geophys. Res. Sp. Phys.*, *119*(2), 1356–1368, doi:10.1002/2013JA019589.

Makela, J. J., J. W. Meriwether, Y. Huang, and P. J. Sherwood (2011), Simulation and analysis of a multi-order imaging Fabry-Perot interferometer for the study of thermospheric winds and temperatures, *Appl. Opt.*, *50*(22), 4403–4416, doi: 10.1364/ao.50.004403.

Mayr, H. G., and I. Harris (1978), Some characteristics of electric field momentum coupling with the neutral atmosphere, *J. Geophys. Res. Sp. Phys.*, *83*(A7), 3327–3336, doi: 10.1029/JA083iA07p03327.

McCormac, F. G., and R. W. Smith (1984), The influence of the interplanetary magnetic field Y component on ion and neutral motions in the polar thermosphere, *Geophys. Res. Lett.*, *11*(9), 935–938, doi:10.1029/GL011i009p00935.

McCormac, F. G., T. L. Killeen, J. P. Thayer, G. Hernandez, C. R. Tschan, J.-J. J. Ponthieu, and N. W. Spencer (1987), Circulation of the polar thermosphere during geomagnetically quiet and active times as observed by Dynamics Explorer 2, *J. Geophys. Res. Sp. Phys.*, *92*(A9), 10,133–10,139, doi:10.1029/JA092iA09p10133.

Meriwether, J. W., J. P. Heppner, J. D. Stolarik, and E. M. Wescott (1973), Neutral winds above 200 km at high latitudes, *J. Geophys. Res.*, *78*(28), 6643–6661, doi: 10.1029/JA078i028p06643.

Niciejewski, R. J., T. L. Killeen, R. M. Johnson, and J. P. Thayer (1992), The behavior of the high-latitude F-region neutral thermosphere in relation to IMF parameters, *Adv. Sp. Res.*, *12*(6), 215–218, doi:10.1016/0273-1177(92)90058-6.

Rees, D., and T. J. Fuller-Rowell (1989), The response of the thermosphere and ionosphere to magnetospheric forcing, *Philos. Trans. R. Soc. London. Ser. A, Math. Phys. Sci.*, *328*(18), 139–171.

Richmond, A. D. (1995), Ionospheric electrodynamics using magnetic apex coordinates., *J. Geomagn. Geoelectr.*, *47*(2), 191–212, doi:10.5636/jgg.47.191.

Richmond, A. D., C. Lathuillere, and S. Vennerstroem (2003), Winds in the high-latitude lower thermosphere: Dependence on the interplanetary magnetic field, *J. Geophys. Res.*,

108(A2), 1066, doi:10.1029/2002JA009493.

Shepherd, G. G., G. Thuillier, Y.-M. Cho, M.-L. Duboin, W. F. J. Evans, W. A. Gault, C. Hersom, D. J. W. Kendall, C. Lathuillère, R. P. Lowe, I. C. McDade, Y. J. Rochon, M. G. Shepherd, B. H. Solheim, D.-Y. Wang, and W. E. Ward (2012), The Wind Imaging Interferometer (WINDII) on the Upper Atmosphere Research Satellite: A 20 year perspective, *Rev. Geophys.*, *50*(2), doi:10.1029/2012RG000390.

Sica, R. J., G. Hernandez, B. A. Emery, R. G. Roble, R. W. Smith, and M. H. Rees (1989), The control of auroral zone dynamics and thermodynamics by the interplanetary magnetic field dawn-dusk (Y) component, *J. Geophys. Res.*, *94*(A9), 11,921, doi:10.1029/JA094iA09p11921.

Sipler, D. P., M. E. Hagan, M. E. Zipf, and M. A. Biondi (1991), Combined optical and radar wind measurements in the F region over Millstone Hill, *J. Geophys. Res.*, *96*(A12), 21,255, doi:10.1029/91JA02371.

Sutton, E. K. (2016), Interhemispheric transport of light neutral species in the thermosphere, *Geophys. Res. Lett.*, doi:10.1002/2016GL071679.

Thayer, J. P., and T. L. Killeen (1991), Vorticity and divergence in the high-latitude upper thermosphere, *Geophys. Res. Lett.*, *18*(4), 701–704, doi:10.1029/91GL00131.

Thayer, J. P., and T. L. Killeen (1993), A kinematic analysis of the high-latitude thermospheric neutral circulation pattern, *J. Geophys. Res.*, *98*(93), 11,549–11,565, doi:10.1029/93JA00629.

Volland, H. (1979), Magnetospheric electric fields and currents and their influence on large scale thermospheric circulation and composition, *J. Atmos. Terr. Phys.*, *41*(7-8), 853–866, doi:10.1016/0021-9169(79)90128-4.

Wharton, L. E., N. W. Spencer, and H. G. Mayr (1984), The Earth's thermospheric superrotation from Dynamics Explorer 2, *Geophys. Res. Lett.*, *11*(5), 531–533, doi:10.1029/GL011i005p00531.

Wu, Q., R. D. Gablehouse, S. C. Solomon, T. L. Killeen, and C.-Y. She (2004), A New Fabry-Perot Interferometer for Upper Atmosphere Research, in *Proc. SPIE*, vol. 5660, edited by C. A. Nardell, P. G. Lucey, J.-H. Yee, and J. B. Garvin, pp. 218–227, doi:10.1117/12.573084.

Wu, Q., D. McEwen, W. Guo, R. Niciejewski, R. Roble, and Y.-I. Won (2008), Long-term thermospheric neutral wind observations over the northern polar cap, *J. Atmos. Solar-Terrestrial Phys.*, *70*(16), 2014–2030, doi:10.1016/j.jastp.2008.09.004.

Moen, J., and A. Brekke (1993), The solar flux influence on quiet time conductances in the auroral ionosphere, *Geophys. Res. Lett.*, *20*(10), 971–974, doi:10.1029/92GL02109.

Ridley, A. J. (2007), Effects of seasonal changes in the ionospheric conductances on magnetospheric field-aligned currents, *Geophys. Res. Lett.*, *34*(5), doi:10.1029/2006GL028444.

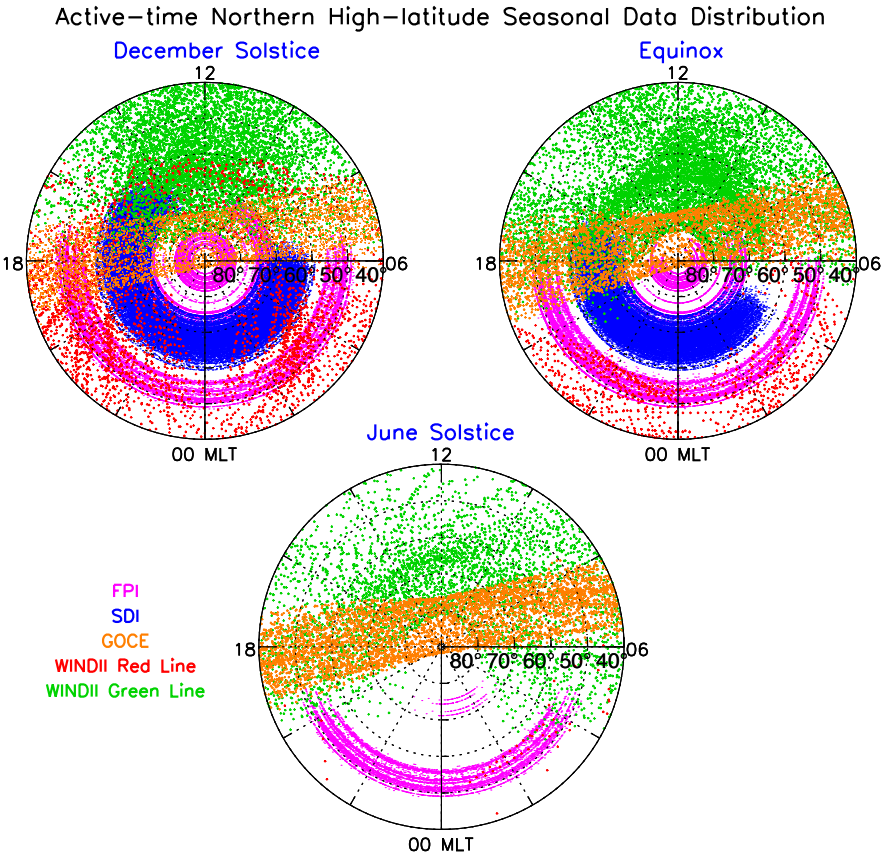

Figure 1. Distribution of the active-time northern hemisphere *F* region thermospheric empirical wind data used in this study as a function of magnetic latitude and magnetic local time. The observational data are divided into three broad seasonal bins: December solstice (Nov, Dec, Jan, Feb), equinox (Mar, Apr, Sep, Oct), and June solstice (May, Jun, Jul, Aug).

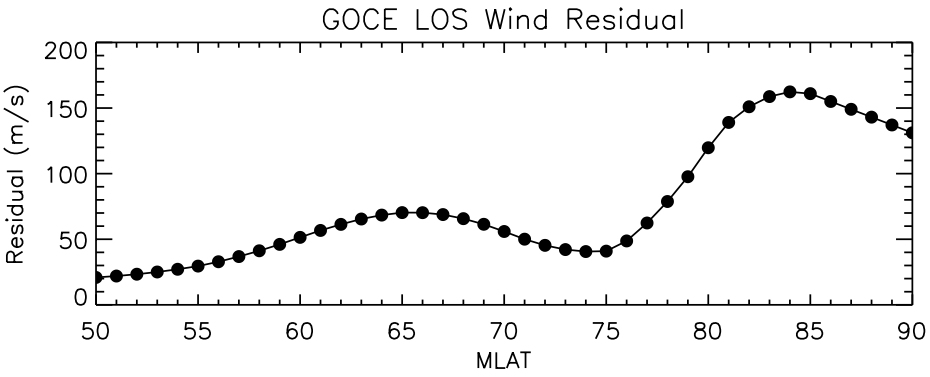

Figure 2. Systematic difference between quiet-time GOCE cross-track winds and quiet-time model climatology without GOCE as a function of magnetic latitude, averaged over all magnetic local times. This quantification of the bias was applied to GOCE data as a correction profile to correct the apparent bias in the GOCE winds.

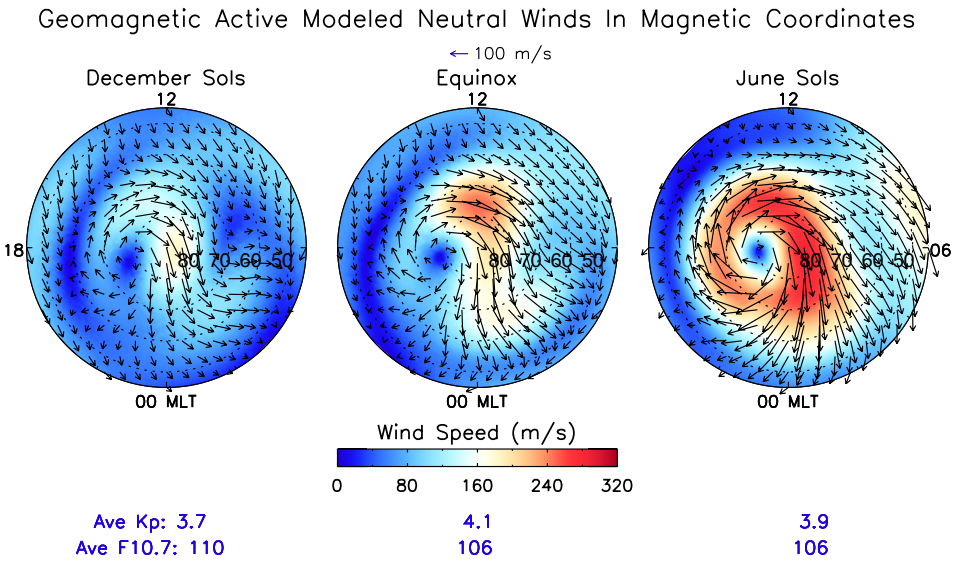

Figure 3. Polar plots of active-time northern high-latitude F region assimilated neutral vector winds as a function of magnetic latitude and magnetic local time (looking down on the geomagnetic north pole). The background color represents the wind speed. Average K_p and $F_{10.7}$ of the data for each season are listed at bottom of each panel. The outer boundary of each panel is located at 45N MLAT.

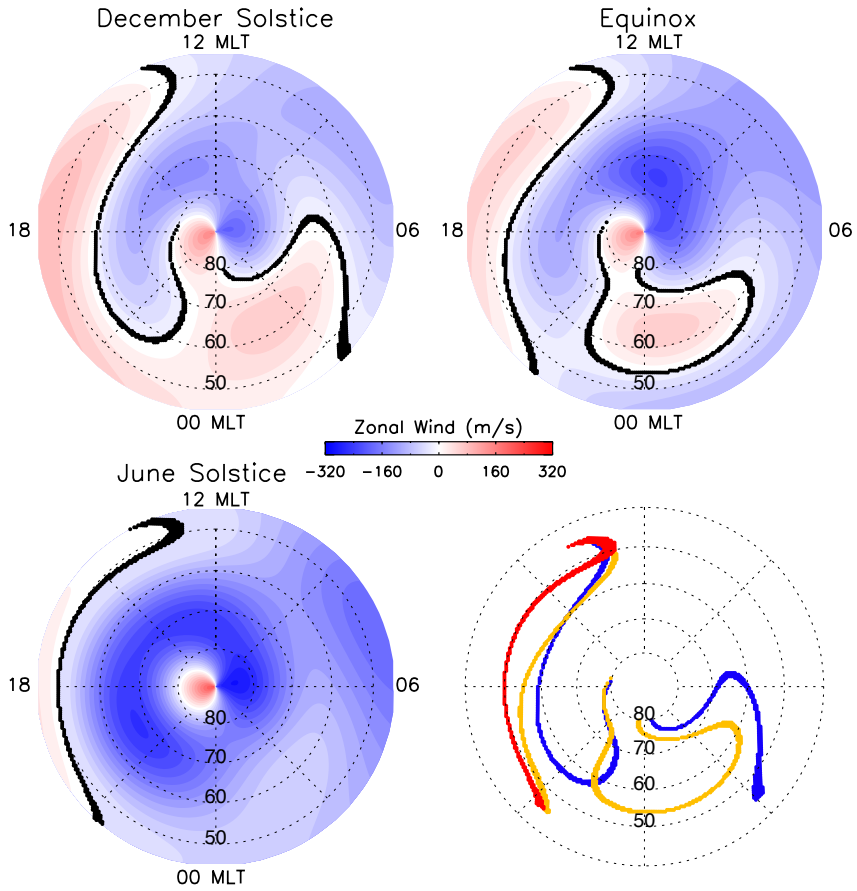

Figure 4. Polar plots of active-time assimilated zonal winds as a function of season, magnetic latitude, and magnetic local time (looking down on the geomagnetic north pole). The black curves in the first three panels represent the boundary between westward (zonal wind negative) and eastward (zonal wind positive) zonal wind flows (wind reversal boundary). For a direct comparison, overpotted wind flow reversal boundaries for December solstice (blue), equinox (yellow), and June solstice (red) are shown in the last panel.

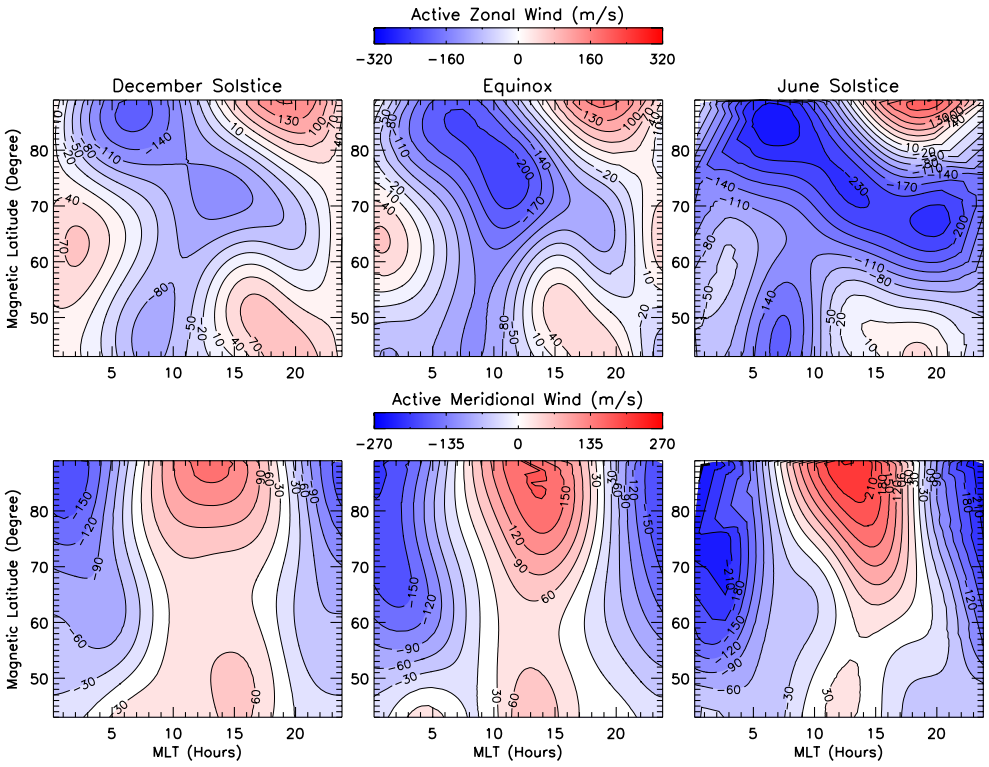

Figure 5. Active-time northern high-latitude *F* region assimilated zonal (top row, positive eastward) and meridional (bottom row, positive northward) wind fields as a function of magnetic local time and magnetic latitude for December solstice (left), equinox (middle), and June solstice (right). Wind contours are separated by 30 m/s.

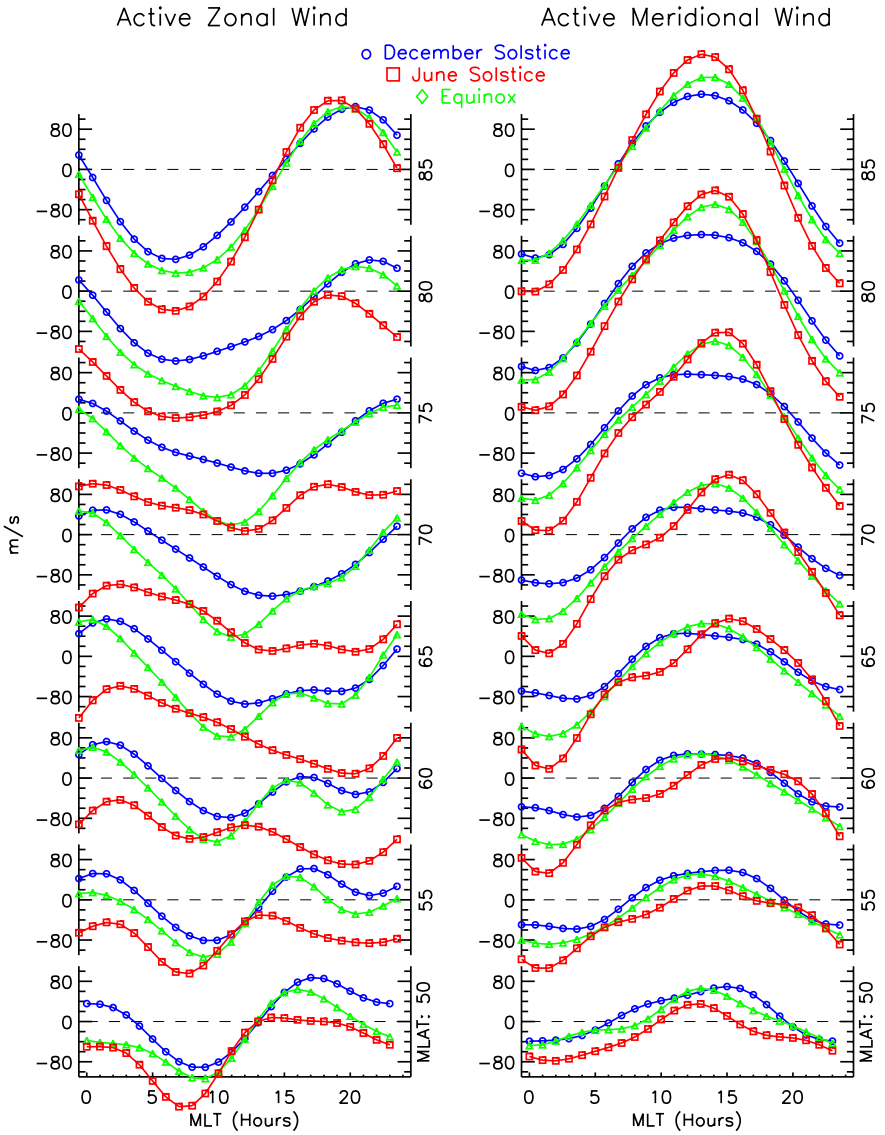

Figure 6. Interseasonal comparison of active-time *F* region assimilated zonal (left) and meridional (right) winds as a function of magnetic local time at various northern high latitudes (annotated on the right y-axis).

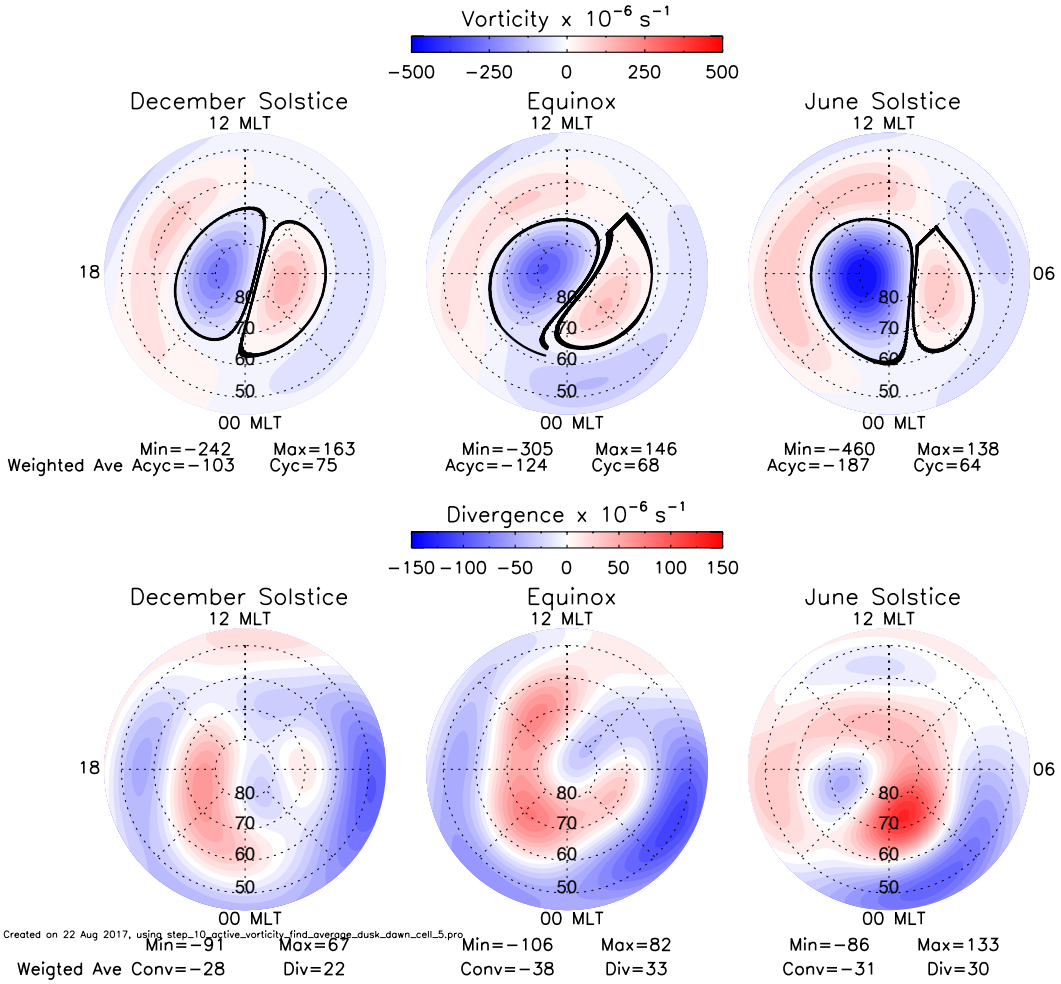

Figure 7. Vorticity (top) and divergence (bottom) of the empirically assimilated active-time northern high latitude *F* region thermospheric vector wind fields as a function of magnetic latitude and magnetic local solar time for December solstice, equinox, and June solstice. For vorticity case, maximum anticyclonic and cyclonic vorticity ($\times 10^{-6}$ s^{-1}) for each season are listed at the bottom of each seasonal panel. The black curves mark the boundary of cyclonic and anticyclonic vortices. The cosine-latitude weighted average vorticity given at the bottom of each panel is calculated for the region inside the black boundaries, which mark the reversal of the sign of the vorticity. For the divergence case, peaks (min and max) and weighted averages are calculated over the entire shown area.

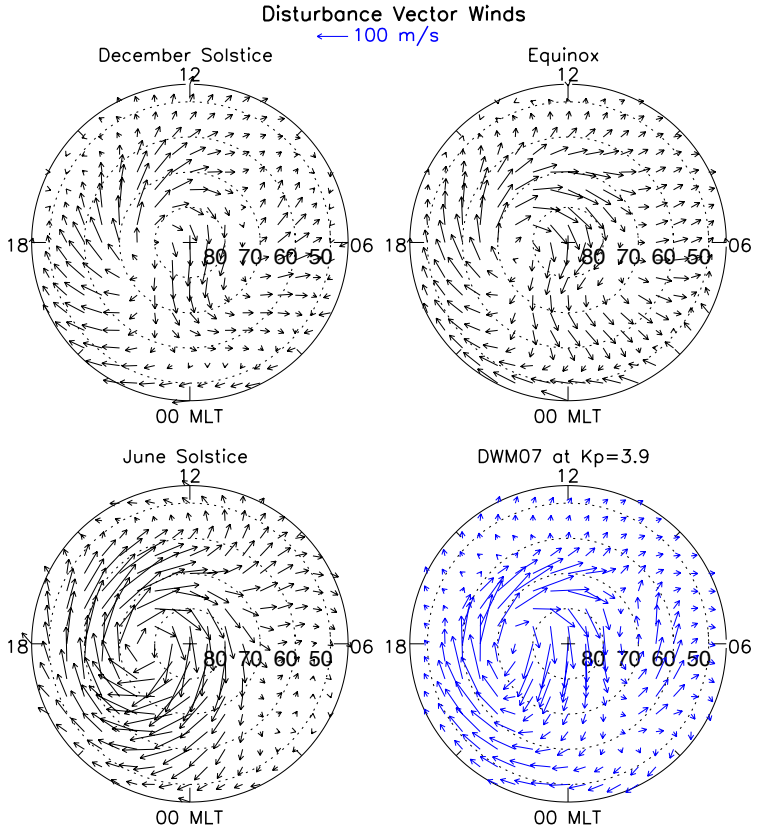

Figure 8. Disturbance vector winds as a function of magnetic latitude and magnetic local time. Figure shows disturbance vector winds for December solstice, equinox, June solstice, and DWM07 (calculated at K_P=3.9). The K_P value (=3.9) used for calculating DWM07 winds is the average of the data used in this study.

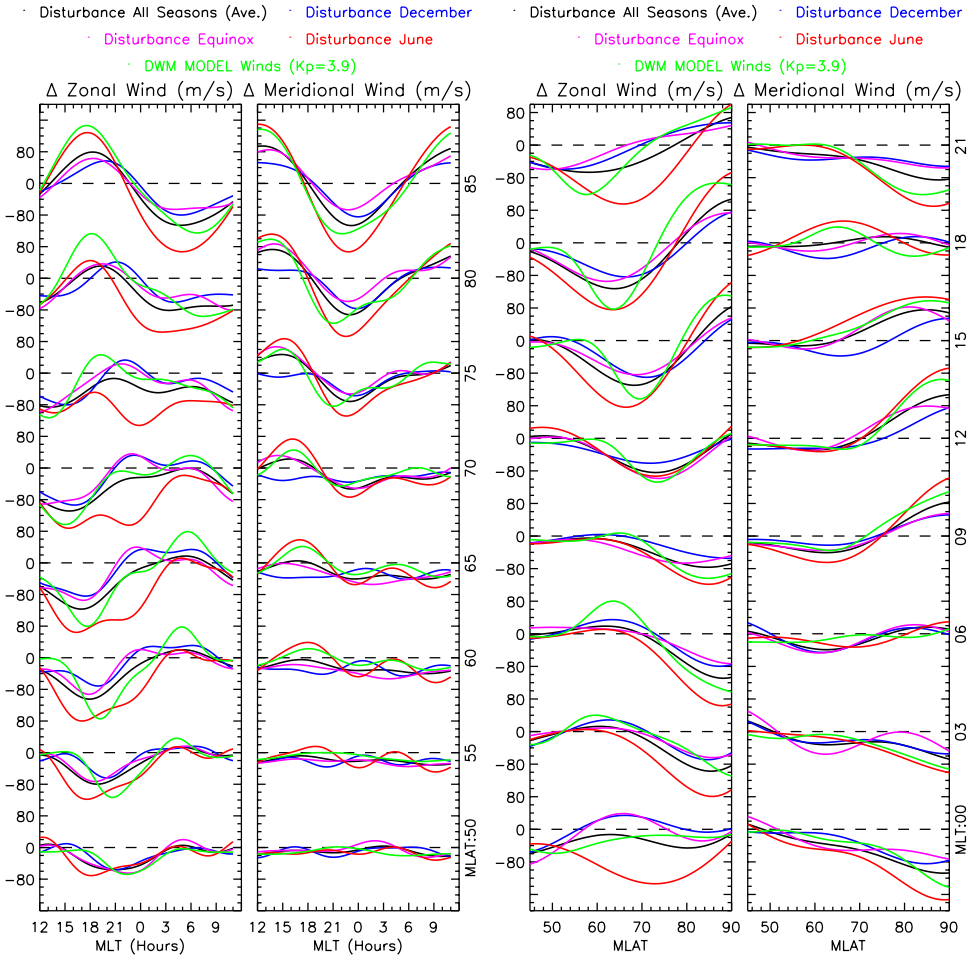

Figure 9. Disturbance zonal and meridional winds as a function of magnetic local time at various northern magnetic high latitudes (left) and as a function of magnetic latitude at various magnetic local times (right). Results are shown for December solstice, equinox, June solstice, and DWM07 (K_p=3.9). The disturbed winds calculated by averaging all the three seasons are also shown.

Table 1. Active time ($K_p \geq 3$) thermospheric horizontal neutral wind data sets used in this study. For space-based instruments, statistics are shown only for the data above 45N magnetic latitude.

Station	Magnetic Latitude	Years of Data	Height (km)	Local Time	Days	Data Points	$<F_{10.7}$ (sfu)>	References
Fabry-Perot Interferometers (ground-based)								
Thule	84.6N	1987	250	night	54	4125	99.01	*Killeen et al.* [1995]
Resolute Bay	83.4N	2003-2012	250	night	234	6576	94.68	*Wu et al.* [2004]
Sndre Strmfjord	73.3N	1983-1984, 1987-1995, 2002-2004	250	night	543	27036	107.0	*Killeen et al.* [1995]
Millstone Hill	53.1N	1990-2002	250	night	420	10121	105.8	*Sipler et al.* [1991]
Peach Mountain	52.1N	2012-2015	250	night	189	12600	113.8	*Makela et al.* [2011]
Urbana	52.1N	2007-2008, 2012-2015	250	night	342	18687	110.3	*Makela et al.* [2011]
Scanning Doppler Imaging Fabry-Perot Interferometers (ground-based)								
Toolik Lake	68.3N	2012-2014	250	night	57	45245	124.1	*Conde and Smith* [1995]
Poker Flat	65.2N	2010-2012	250	night	84	46309	114.1	*Conde and Smith* [1995]
Space-based Instruments								
WINDII 557.7 nm	81.6N-88.0S	1991-1997	210-320	day	262	17635	96.90	*Shepherd et al.* [2012]
WINDII 630.0 nm	80.1N-86.0S	1991-1997	210-320	night	83	3107	98.09	*Shepherd et al.* [2012]
GOCE	90.0N-89.8S	2009-2012	253-295	twilight	279	10907	103.8	*Doornbos et al.* [2014]